Environmental Science & Technology

Article

Cite This: Environ. Sci. Technol. 2018, 52, 12349−12357

pubs.acs.org/est

Manganese-Driven Carbon Oxidation at Oxic−Anoxic Interfaces

Morris E. Jones,[†] Peter S. Nico,[‡] Samantha Ying,[§] Tom Regier,[∥] Jürgen Thieme,[⊥] and Marco Keiluweit*,[†]

[†]School of Earth & Sustainability and Stockbridge School of Agriculture, University of Massachusetts, Amherst, Massachusetts 01003, United States

[‡]Earth and Environmental Sciences Area, Lawrence Berkeley National Laboratory, Berkeley, California 94720, United States

[§]Department of Environmental Sciences, University of California Riverside, Riverside, California 92521, United States

[∥]Canadian Synchrotron Lightsource, Saskatoon, Canada

[⊥]NSLS-II, Brookhaven National Laboratory, Brookhaven, New York 11973, United States

Supporting Information

ABSTRACT: The formation of reactive manganese (Mn) species is emerging as a key regulator of carbon oxidation rates, and thus CO_2 emissions, in soils and sediments. Many subsurface environments are characterized by steep oxygen gradients, forming oxic−anoxic interfaces that enable rapid redox cycling of Mn. Here, we examined the impact of $Mn(II)_{aq}$ oxidation along oxic−anoxic interfaces on carbon oxidation in soils using laboratory-based diffusion reactors. A combination of cyclic voltammetry, X-ray absorption spectroscopy, and X-ray microprobe imaging revealed a tight coupling between $Mn(II)_{aq}$ oxidation and carbon oxidation at the oxic−anoxic interface. Specifically, zones of $Mn(II)_{aq}$ oxidation across the oxic−anoxic transition also exhibited the greatest lignin oxidation potential, carbon solubilization, and oxidation. Microprobe imaging further revealed that the generation of Mn(III)-dominated precipitates coincided with carbon oxidation. Combined, our findings demonstrate that biotic $Mn(II)_{aq}$ oxidation, specifically the formation of Mn(III) species, contributes to carbon oxidation along oxic−anoxic interfaces in soils and sediments. Our results suggest that we should regard carbon oxidation not merely as a function of molecular composition, which insufficiently predicts rates, but in relation to microenvironments favoring the formation of critically important oxidants such as Mn(III).

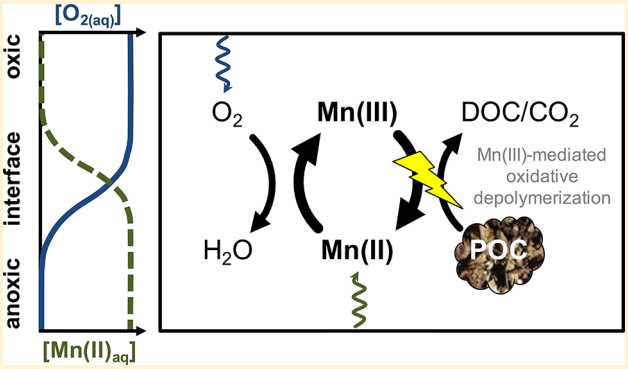

INTRODUCTION

Oxidative degradation pathways of particulate organic carbon (POC) in soils and sediments determine the proportion of carbon (C) that is either stored or emitted to the atmosphere as CO_2.[1] Even a small increase in C oxidation rates may thus cause adverse feedback to the climate system.[2] POC is derived from foliar and root tissue, and its oxidation rate has long been linked to climatic predictors such as temperature and moisture, but also chemical properties such as lignin content.[3] Lignin—an aromatic biomacromolecule—often makes up between 20% and 60% of POC because it is concentrated in plant cell walls.[4] It encrusts cellulose microfibrils to form protective physical units that are embedded in a matrix of hemicellulose. Full conversion of POC into CO_2 necessitates oxidative mechanisms that depolymerize these complex biopolymers into smaller, soluble monomers that can be assimilated by microbes. These mechanisms rely on the production of oxidants that are potent and small enough to penetrate intact macromolecular structures. Understanding of the environmental factors that regulate the formation of suitable oxidants is therefore critical for predictions of POC oxidation rates.

Manganese (Mn) appears to be a particularly important driver of POC oxidation. Numerous studies found strong positive correlations between Mn abundance and the rate of POC oxidation in boreal, temperate, and semiarid soils.[5−8] Among all other parameters tested, Mn concentration best predicted POC oxidation rates, leading researchers to conclude that Mn concentration is the single main factor governing POC degradation.[9] However, efforts to examine the effect of Mn availability on POC oxidation have produced ambiguous results,[10] likely caused by the fact that the experimental conditions did not allow for active Mn redox cycling. Resolving the mechanism underlying this apparent "Mn-dependence" of POC oxidation

Received: July 11, 2018
Revised: September 26, 2018
Accepted: September 27, 2018
Published: September 27, 2018

DOI: 10.1021/acs.est.8b03791
Environ. Sci. Technol. 2018, 52, 12349−12357

requires consideration of redox conditions promoting the formation of Mn-based oxidants.

Several lines of evidence suggest that $Mn(II)_{aq}$ oxidation, particularly the formation of ligand-stabilized Mn(III), facilitates the degradation of biomacromolecules such as lignin. For example, oxidation of $Mn(II)_{aq}$ to Mn(III) by fungal peroxidase enzymes coincides with the degradation of lignin model compounds.[11] When stabilized by chelating ligands such as organic acids, these soluble Mn(III)−ligand complexes are thought to act as potent oxidants.[12] $Mn(III)_{aq}$ is small enough to penetrate intact macromolecular structures such as POC, which may offer a great advantage over larger oxidative enzymes[12] or solid Mn(III,IV) oxide surfaces with oxidative potential.[13] Using spectroscopic and microscopic tools, we recently demonstrated a link between $Mn(II)_{aq}$ oxidation and microbial POC degradation in soils.[14] Moreover, it is important to note that $Mn(II)_{aq}$ oxidation is not limited to fungal peroxidases; it is also catalyzed by multicopper oxidases (or laccases) produced by a diverse range of fungi and heterotrophic bacteria.[15−17] In spite of this widespread physiological potential for microbial $Mn(II)_{aq}$ oxidation, the environmental conditions favoring the formation of Mn(III)-based oxidants in soils remain largely unknown.

To date, information on the formation of dissolved Mn(III) *in situ* is limited to marine environments. Using a novel spectrophotometric approach to quantifying soluble Mn(III)−ligand complexes, Madison et al.[18] detected this transient and reactive Mn species along redox gradients in aquatic and sedimentary systems for the first time. Most importantly, the greatest $Mn(III)_{aq}$ concentrations were found at the oxic−anoxic boundary, suggesting that soluble Mn(III)−ligand complexes rely on the presence of oxygen near the interface. Dissolved Mn(III) concentrations also appear to be particularly elevated in the presence of strong organic ligands.[19,20] Geochemical modeling further indicated that $Mn(III)_{aq}$ formation is proportional to the diffusive flux of $Mn(II)_{aq}$, generated in the anoxic zone, toward the oxic−anoxic boundary. In sum, these observations were taken as evidence that Mn(III) is primarily formed by oxidative as opposed to reductive pathways.

In soils, $Mn(II)_{aq}$ oxidation at oxic−anoxic interfaces appears to be biologically mediated. For example, Thompson et al.[21] observed that soil-borne fungi preferentially colonize the suboxic zone and rapidly oxidize $Mn(II)_{aq}$ to Mn(III/IV) oxides. Here fungi appeared to harness $Mn(II)_{aq}$ generated through Mn(III/IV) reduction in the anoxic zone, while maintaining access to O_2 from the oxic zone at the same time. It is well-known that the spatial architecture of soils and sediments creates a mosaic of redox gradients,[22] resulting in sharp oxic−anoxic transitions even in well-drained upland soils.[23] Such oxic−anoxic interfaces are increasingly recognized as "hotspots" for microbial activity[24] and C oxidation,[25] but the underlying mechanisms are not well understood.[26] Here, we asked if biotic $Mn(II)_{aq}$ oxidation at oxic−anoxic interfaces, and the resulting formation of reactive Mn(III) species, would enhance POC degradation.

The overall objective of this study was to determine the effect of $Mn(II)_{aq}$ oxidation at oxic−anoxic interfaces on POC degradation. We hypothesized that $Mn(II)_{aq}$ and oxygen gradients would overlap at the oxic−anoxic interface, promoting biotic Mn oxidation that would lead to the solubilization and oxidation of POC. We tested this hypothesis by incubating POC (leaf litter) in mineral soil packed into a diffusion reactor system designed to establish stable oxic−anoxic transitions.[27] After 30 days, we recorded fine scale gradients in dissolved O_2 and $Mn(II)_{aq}$ concentration using cyclic voltammetry,[28] and analyzed changes in bulk Mn and C chemistry across the interface using wet-chemical extractions and synchrotron-based X-ray absorption near edge fine structures (XANES) spectroscopy. Finally, we used a novel, multimodal imaging approach, combining soft and hard X-ray microprobe analysis of the same samples, to determine if hotspots of $Mn(II)_{aq}$ oxidation are also sites of enhanced POC oxidation.

MATERIALS AND METHODS

Soil Samples. To conduct laboratory experiments with environmentally relevant POC in soil, we collected leaf litter and mineral soil material at the Harvard Forest Long-term Ecological Research site near Petersham, Massachusetts (42.54° N, 72.18° W). Samples were collected at the transition between the upland and wetland soils that undergo frequent redox cycles.[29] Soils are sandy loams classified as *Typic Dystrudepts* of the Gloucester series. The secondary forest is dominated by red oak (*Quercus rubra*), paper birch (*Betula papyrifera* M.), red and striped maple (*Acer rubrum* L., *Acer pennsylvanicum* L.), and white ash (*Fraxinus americana* L.), which supply the majority of the leaf litter. Leaf litter and A-horizon mineral soil (0−10 cm) samples were collected and air-dried. Coarse roots and twigs were removed before samples were ground and sieved to 2000−590 μm for litter and 590−53 μm for A-horizon soil. The pH of the litter was 3.8 and that of the mineral soil 4.4. Extractable and total metal concentrations of the composite sample used for reactor experiments are given in Table S-1.

Reactor Experiment. To create a stable oxygen gradient along which $Mn(II)_{aq}$ oxidation could be studied, a modified diffusion reactor was used.[27] Reactors consist of a polycarbonate chamber (10 × 8 × 1 cm) with an open top to allow oxygen diffusion into the surface soil. The reactor has an inlet at the bottom of the chamber equipped with a tensiometer consisting of a ceramic cup (Soil Moisture Equipment, Santa Barbara CA) to regulate water table height.[21] To amend soil containing reducible Mn oxides with fresh litter, equal masses of litter and A horizon soil were mixed and dry-packed into the reactors. Reactors were hydrated with deionized water through the inlet, and the water table was maintained at 1 cm below the soil surface for the duration of the experiment. Triplicate reactors were incubated in the dark at 23 °C until the oxic−anoxic interface showed visible colonization by fungi at 30 days.

Electrochemistry. At the end of the incubation period, *in situ* electrochemical profiles of $O_{2(aq)}$, $Mn(II)_{aq}$, and $Fe(II)_{aq}$ were recorded across the oxic−anoxic transition using solid-state mercury/gold (Hg/Au) voltammetric microelectrodes. Hg/Au microelectrodes were constructed as previously reported[28] and used with stationary Ag/AgCl reference and platinum (Pt) counter electrodes placed 1 mm below the sediment surface. All measurements were made with a DLK-70 potentiostat (Analytical Instruments Systems, Ringoes, NJ). $O_{2(aq)}$ was quantified by linear sweep voltammetry (LSV), between −0.1 and −1.9 V at a scan rate of 100 mV/s with a 10 s deposition at −0.1 V. $Mn(II)_{aq}$ and $Fe(II)_{aq}$ were measured by square-wave voltammetry (SWV), between −0.1 and −1.9 V at a scan rate of 200 mV/s with a 10 s deposition at −0.1 V. For each reactor, duplicate LSV and SWV voltammograms were measured at 0.5 mm increments to a depth of 25 mm using a micromanipulator (Analytical Instrument Systems, Inc., Ringoes, NJ). Voltammograms were integrated using the

DOI: 10.1021/acs.est.8b03791
Environ. Sci. Technol. 2018, 52, 12349−12357

VOLTINT software package.[30] Electrodes were calibrated with a $MnCl_2$ solution, and $Fe(II)_{aq}$ was determined by the pilot ion method.[28,31] $O_{2(aq)}$ porewater concentrations were calibrated using fully saturated and degassed 0.05 M NaCl solutions at 23 °C.

Reactor Sampling. After 30 days of incubation, reactors were dismantled in a N_2/H_2(97%:3%) atmosphere anaerobic chamber (Coy Laboratory Products Inc., Ann Arbor, MI). On the basis of the electrochemical profiles, the soil column was divided into aerobic (0−2 mm), transition (2−7 mm), and anaerobic (7−25 mm) zones and sampled accordingly. Soils retrieved from the individual zones were dried in the anaerobic chamber, homogenized, and stored in the dark until further use. In addition, a 1 × 1 × 4 cm core was taken across the oxic−anoxic transition, fully hydrated under a vacuum, flash-frozen in liquid N_2, cryosectioned on a cryostat (Leica CM1950, Leica Biosystems, Nussloch, Germany), and mounted on glass slides for chemical imaging as described in ref 14. This approach allowed for the generation of thin sections without the use of organic resins that would interfere with the characterization of changes in the C chemistry. Thin sections were stored anaerobically in the dark prior to analysis by X-ray microprobe.

Sequential Dissolution. Changes in the abundance of solid Mn phases of various crystallinity across the redox transition were assessed by sequential extraction of solid samples. Extraction by ultrapure H_2O ("water-soluble Mn") was followed by acidified hydroxylamine ("easily reducible Mn,"[32]) and dithionite-HCl ("total reducible Mn,"[33]). Briefly, 0.33 g of dried reactor soil was added to 15 mL centrifuge tubes with 10 mL of ultrapure H_2O (18.3 M-ohm). Extracts were shaken for 1 h at 120 rpm, followed by centrifugation (1 h at 4000 RCF) and filtration of the supernatant through 0.22-μm syringe filters. The remaining soil pellet was resuspended in 10 mL of 0.25 M hydroxylamine hydrochloride in 0.25 M hydrochloric acid, shaken for 4 h (120 rpm), and centrifuged (1 h at 4000 RCF). Residues were rinsed with 10 mL of deionized water, and combined extracts were filtered. The remaining soil pellet was resuspended in 10 mL of 0.05 M sodium dithionate, shaken for 16 h (120 rpm), centrifuged (1 h at 4000 RCF), and filtered. The residues were washed with 0.05 M HCl for 1 h, centrifuged, filtered, and combined with the dithionite extract. All extracts were acidified with 3% HNO_3 and analyzed for Al, Fe, and Mn by ICP-MS (Shimadzu ICPMS-2030). Organic C concentrations in the H_2O extracts were measured on a total organic carbon analyzer (Shimadzu TOC-L). All extractions were carried out in duplicate.

Lignin Oxidation Potential. The oxidative potential for lignin-like compounds in each redox zone was examined using L-3,4-dihydroxyphenylalanine (L-DOPA) as a probe. Substrate oxidation was examined in duplicate soil slurries in the presence and absence of hydrogen peroxide (H_2O_2) as described in Bach et al.[34] and recorded using a microplate spectrophotometer (Epoch 3, Biotek Instruments, Winooski, VT).

Mn and C X-ray Absorption near-Edge Spectroscopy (XANES). To determine average Mn oxidation, solid samples were analyzed by Mn K-edge XANES at the wiggler beamline 4−3 at the Stanford Synchrotron Radiation Lightsource. Triplicate samples were homogenized and combined into one-composite samples (at a 1:1:1 mass ratio) and mounted in sample holders, sealed with X-ray transparent Kapton tape, and stored anaerobically prior to analysis. Spectra were calibrated, background corrected, and normalized,[35] and a linear combination fitting procedure was used to obtain the relative abundance of Mn(II), Mn(III), and Mn(IV), as well as the Mn average oxidation state (Mn_{AOS}).[35] Changes in C functional group distribution and oxidation state were determined by C (1s) K-edge XANES at the SGM beamline at the Canadian Light Source (CLS).[36] Samples were analyzed, normalized, and deconvoluted as described in ref 27.

X-ray Microprobe Imaging. To determine Mn distribution and oxidation state across the oxic−anoxic transitions, a soil thin section taken across the interface was analyzed by both soft and hard X-ray microprobes. A representative thin section was first analyzed using the new soft X-ray microprobe capability at the SGM beamline. Using the microprobe, C μXANES were recorded at various locations across the interface, focusing on regions around the black band of potential Mn precipitates. The beam was focused to a spot size of 25 μm, and each scan was collected in "sweep" mode over the course of 1 min. To enhance the signal-to-noise ratio and minimize beam damage, the beam was moved in 25-μm steps across a 3 × 3 raster, and a total of nine scans were collected. Each spectrum thus represents the average of nine scans collected across a 75 × 75 μm sized region and was subsequently processed as described above.

Elemental maps and Mn μXANES spectra of the same thin section were obtained by subsequent analysis at the hard X-ray microprobe beamline 5-ID (SRX) of the National Synchrotron Light Source II at the Brookhaven National Laboratory. X-ray fluorescence maps were recorded by raster scanning the sample with the incident X-ray energy at 6000 (for Mn and Ca) and 7000 (for Fe) eV with a spot size of 2 μm and a dwell time of 50 ms. The full XRF spectrum at each point (pixel) was recorded with a silicon drift detector. Several regions of interest were selected from the XRF maps for Mn K-edge μXANES analysis. Fluorescence yield was recorded, and the resulting spectra were calibrated and normalized as described above.

RESULTS

Electrochemical Profiles. Microelectrode measurements of soil incubated in our reactors for four weeks confirmed the presence of pronounced $[O_2]_{aq}$ and $[Mn(II)]_{aq}$ gradients (Figure 1). While $[O_2]_{aq}$ was depleted within the first 5 mm

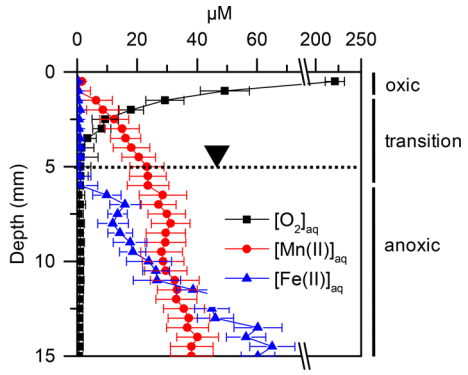

Figure 1. Electrochemistry profiles of dissolved O_2, Mn(II), and Fe(II) concentrations across the soil column. Depth is measured relative to the surface of the soil column in the reactor. Profiles represent the average of three replicate reactors, with error bars denoting the standard error of the mean. "Oxic," "transition," and "anoxic" zones were sampled for solid phase analysis. The position of the stationary water table is indicated by the dotted line.

below the soil surface, $[Mn(II)]_{aq}$ began to continuously rise at around 2 mm depth, and $[Fe(II)_{aq}]$ was present only at depths

DOI: 10.1021/acs.est.8b03791
Environ. Sci. Technol. 2018, 52, 12349−12357

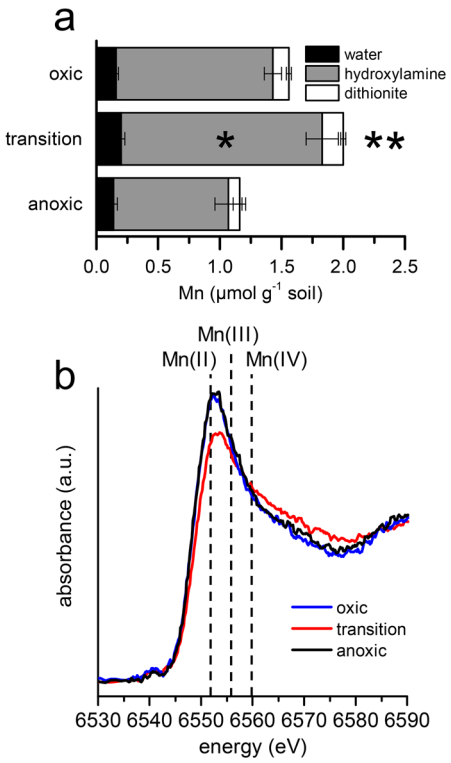

Figure 2. Changes in Mn chemistry across the oxic–anoxic interface as determined by (a) selective dissolution using water, hydroxylamine, and dithionite-HCl and (b) Mn K-edge X-ray absorption near-edge spectroscopy (XANES) spectra of bulk samples from each zone. For comparison, extractable Al and Fe concentrations are shown in Figure S-2. Both hydroxylamine (*$p < 0.05$) and total extractable Mn (**$p < 0.01$) are significantly more abundant in the transition zone (one-way ANOVA, Tukey's HSD).

greater than 6 mm (Figure 1). The observed gradients are generally consistent with the notion that Mn and Fe oxidation and reduction occur in distinct redox zones, with Mn oxidation/reduction occurring closer to the oxic zone than Fe oxidation/reduction.[37] These results also suggested that there is a narrow transition zone at depths between 2 and 6 mm in which both $O_{2(aq)}$ and $Mn(II)_{aq}$ are present. On the basis of these data, we assumed that this transition zone would exhibit the greatest potential for $Mn(II)_{aq}$ oxidation on POC degradation, with limited effects from $Fe(II)_{aq}$-mediated oxidation reactions.[38,39] To quantify $Mn(II)_{aq}$ oxidation and its impact on POC oxidation within that transition zone, we sampled from this depth (2–6 mm), as well as depths corresponding to aerobic (0–2 mm) and anaerobic zones (6–20 mm; Figure 1).

Mn Chemistry Across the Oxic–Anoxic Interface. Wet-chemical extractions as well as Mn XANES showed that oxidized Mn phases accumulated in the transition zone during the incubation (Figure 2). The transition zone showed significantly greater amounts of total reducible (dithionite-extractable) Mn compared to both oxic and anoxic zones (Tukey's HSD, $p < 0.01$), an increase that was largely driven by significant increases in the easily reducible (hydroxylamine-extractable) Mn pool (Tukey's HSD, $p < 0.05$; Figure 2a). Although extractable Fe and Al concentrations were generally higher than those of Mn, we found no significant accumulation of total extractable Fe and Al in the transition zone relative to the other zones (Figure S-2). Corresponding bulk Mn XANES of each zone showed a shift of the edge position toward higher energies (Figure 2b) indicative of a higher Mn oxidation state.[35] A higher average Mn oxidation state (Mn_{AOS}) in the transition zone was corroborated using linear combination fitting (LCF),[14,35] which showed that Mn_{AOS} increased from ~2.3 in both aerobic and anaerobic zones to ~2.6 in the transition zone (Table 1). LCF results indicated that this increase in Mn_{AOS} is driven by a ~50% increase in the relative abundance of Mn(III) and M(IV) (Table 1), with Mn(III) and Mn(IV) maintaining approximately a 2:1 ratio. Although identifying the underlying $Mn(II)_{aq}$ oxidation pathways was beyond the scope of this paper, visual inspection of the transition zone showed dense growth of fungal hyphae associated with dark clusters of black precipitates resembling Mn(III,IV) oxides (Figure S-2). Taken together, chemical extraction and XANES results suggest that dissolved $Mn(II)_{aq}$ produced by reductive processes in the anaerobic zone and supplied via diffusion (Figure 1) is potentially subjected to microbially mediated oxidation at the oxic–anoxic interface, resulting in the accumulation of Mn oxide phases dominated by Mn(III).

C Chemistry Across the Oxic–Anoxic Interface. Enhanced $Mn(II)_{aq}$ oxidation in the transition zone coincided

Table 1. Fitting Results for Mn and C XANES Collected by Bulk X-ray Absorption Spectroscopy and X-ray Microprobe

location	Mn K-edge XANES				C K-edge XANES						
	Mn(II)	Mn(III)	Mn(IV)	Mn_{AOS}[a]	aromatic	phenolic	aliphatic	carboxylic	alkyl	carbonyl	C_{ox}[a]
	rel. abundance (%)				rel. abundance (%)						
(a) bulk X-ray Absorption Spectroscopy											
oxic	77	16	8	2.31	15	11	11	30	20	13	2.0
transition	58	28	14	2.57	13	11	10	32	20	14	2.4
anoxic	79	14	7	2.28	15	11	11	31	19	13	2.0
(b) X-ray microprobe											
transition zone (+Mn)[b]	71	27	2	2.31	18	8	16	28	24	6	1.6
transition zone (-Mn)[c]	87	10	3	2.16	20	9	16	25	23	6	1.3
oxic + anoxic zone[d]	88	8	4	2.15	21	8	17	26	22	6	1.2

[a]Mn_{AOS} = Mn average oxidation state; C_{ox} = absorbance of carboxylic C (288.3 eV) divided by absorbance of aromatic C (285 eV) [b]Average fit results for Mn μ-XANES collected at locations 1–3 within the transition zone characterized by black precipitates (Figure 4b). C μ-XANES were collected from two locations with black precipitates along the transition (locations 1 and 2 in Figure 4a). [c]Averaged fit results for Mn μ-XANES collected at locations 4–6 within the transition zone showing no black precipitates (Figure 4b). C μ-XANES were collected from two locations without black precipitates along the transition zone (locations 3 and 4 in Figure 4a). [d]Averaged fit results for Mn μ-XANES collected at locations 7–9 within oxic and anoxic zones with no signs of Mn precipitation (Figure 4b). C μ-XANES were collected from locations in the oxic and anoxic zone (locations 5 and 6 in Figure 4a).

DOI: 10.1021/acs.est.8b03791
Environ. Sci. Technol. 2018, 52, 12349–12357

with greater POC solubilization and oxidation (Figure 3). Oxidation rates for the lignin model compound L-DOPA in

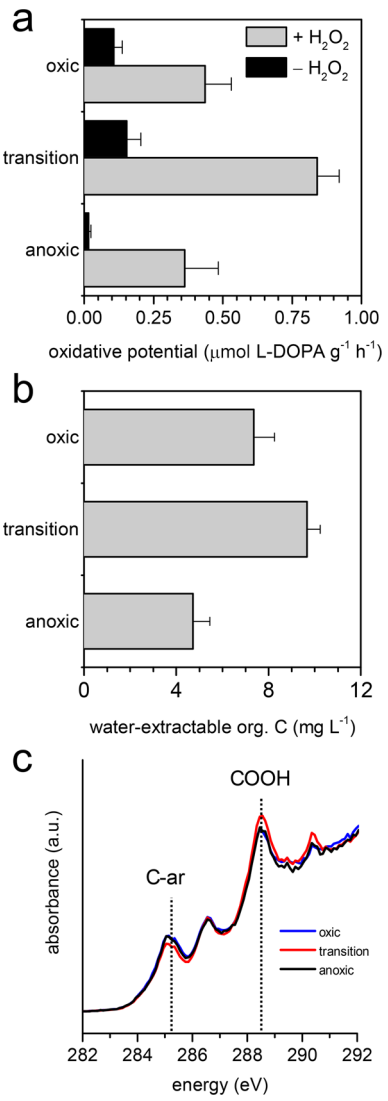

Figure 3. Carbon oxidation across the interface. Changes in (a) oxidative potential for lignin analogue L-3,4-dihydroxyphenylalanine (L-DOPA), (b) the amount of water extractable organic C, and (c) chemical composition of solid-phase C as determined by C K-edge X-ray absorption near-edge spectroscopy (XANES) across the interface.

the transition zone were significantly greater than in aerobic and anaerobic zones both in the presence and absence of H_2O_2 (Figure 3a). Correspondingly, the amount of water extractable C was significantly greater within the transition zone, suggesting that the elevated lignin oxidation potential in the transition zone resulted in POC depolymerization and production of soluble compounds. C XANES further showed that this increase in soluble organic compounds in the transition zone was accompanied by a decline in the absorbance of aromatic C and an increase in the absorbance of carboxylic C relative to the other zones (Figure 3c and Table 1). Consequently, the ratio of C-OOH/C-ar, used as a proxy for C oxidation state (C_{ox}), increased from ~2 in both anaerobic and aerobic zones, to ~2.4 in the transition zone (Table 1). While these changes are relatively modest possibly due to the short incubation time (30 days), our findings suggest that the formation and accumulation of reactive Mn(III,IV) species in the transition zone caused POC degradation that led to more depolymerized and/or oxidized products. To further corroborate the coupling of Mn and C cycles across the interface, we applied a multimodal imaging approach to visualize the co-occurrence of Mn(III) formation with POC oxidation on the micron-scale.

Micron-Scale Analysis of Colocalized Mn and C Oxidation. Combining hard and soft X-ray microprobe imaging to visualize both Mn and C chemistry across the oxic–anoxic interface revealed that Mn(III) phases and oxidized POC are colocalized (Figure 4 and 5). Microscopic examination of thin sections across all three redox zones revealed a dark narrow band of black precipitates within the transition zone (Figure 4a). Elemental maps collected of a representative thin section by XRF show consistently elevated Mn concentrations within the dark band (Figure 4b). Comparison of Mn, Fe, and Ca intensities across the transects interface to an untreated control show notably greater enrichment for Mn than for Fe and Ca (Figure S-3).

Mn μXANES were collected across the band of Mn enrichments from regions with higher (+Mn, spots 1–3) and lower Mn concentrations (–Mn, spots 4–6), as well as regions in both the oxic and anoxic zones (spots 7–9; Figure 4b). The resulting spectra (Figure 5) of the dark precipitates (+Mn, spots 1–3) showed stronger absorption at higher energies than spectra collected from adjacent locations with less Mn (–Mn, spots 4–6) or locations in oxic and anoxic regions. LCFs of the Mn XANES further show that that between 14 and 29% of the Mn within dark, Mn rich regions (+ Mn, spots 1–3) can be attributed to Mn(III) (Table 1). LCFs of Mn μXANES from locations without noticeable Mn accumulation (–Mn), as well as those collected from aerobic and anaerobic zones, did not show any evidence of oxidized Mn (Table 1).

Corresponding C μXANES spectra, collected from locations identified in Figure 4a, show that Mn-rich locations (+Mn) have a lower abundance of aromatic C and a higher abundance of carboxylic C/amide C than less Mn-rich regions in the transition zones (–Mn) or the oxic/anoxic regions (Figure S-4). Consequently, the ratio of carboxyl C/aromatic C, again used as a proxy for degree of C oxidation state (C_{ox}), of the C associated with Mn-rich hotspots (~1.6) was greater than in regions without Mn accumulation in transition, anaerobic, and aerobic zones (~1.2; Table 1). Combined, both soft and hard X-ray microprobe imaging and μXANES suggest that $Mn(II)_{aq}$ oxidation in the transition zone created a narrow band of Mn(III)-rich precipitates, the formation of which facilitated the oxidation of POC.

DISCUSSION

Along a soil redox gradient, oxidative degradation of POC was greater within the transition zone than in either oxic or anoxic zones (Figure 3 and Table 1). This result is surprising given that one might expect the greatest oxidative potential for POC degradation in the oxic zone, rather than the transition zone where O_2 supply is limited. However, it is consistent with recent observations of elevated microbial activity and C oxidation at oxic–anoxic interfaces,[24,25] suggesting that factors other than O_2 availability may also regulate oxidative decay rates. Our results showed that enhanced POC degradation at the oxic–anoxic transition coincided with $Mn(II)_{aq}$ oxidation and the associated formation of Mn(III) species. Dissolved Mn(II), provided by reductive dissolution in the anaerobic zone, was delivered to the interface via diffusion along a concentration

DOI: 10.1021/acs.est.8b03791
Environ. Sci. Technol. 2018, 52, 12349–12357

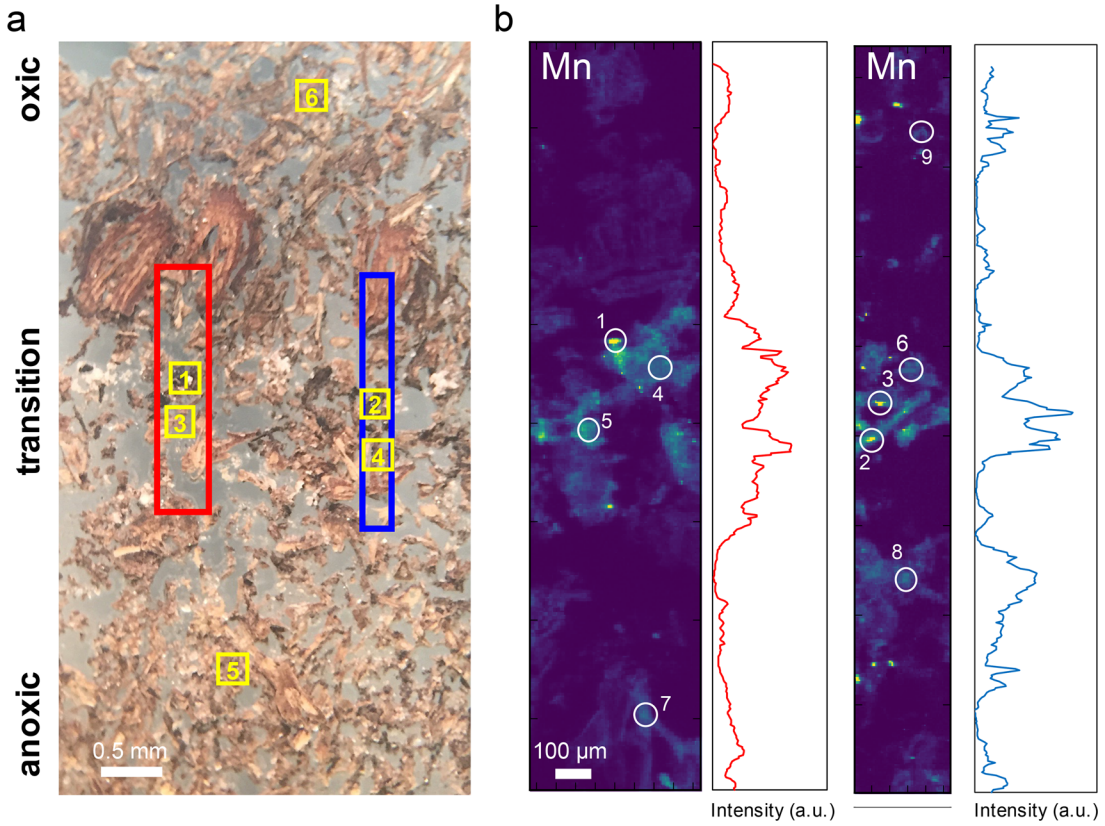

Figure 4. Micron-scale Mn distribution across oxic−anoxic interfaces. (a) Light microscope image of thin section across the oxic−anoxic interface. Note the band of black precipitates along the transition zones. Red and blue boxes denote regions used for XRF mapping of Mn distribution. Yellow squares denote regions used to collect C μXANES. Squares 1 and 2 mark locations with black precipitates along the transition, squares 3 and 4 mark locations along the transition without black precipitates, and squares 5 and 6 mark locations in oxic and anoxic zones. (b) Mn maps across the interface for the two regions of interest (red and blue) identified in a. White circles denote locations for which Mn μXANES were collected. Locations with high (+Mn, circles 1−3) and low Mn (−Mn, circles 4−6) concentrations were targeted along the transition zone. μM XANES were also collected of locations outside of the transition zone (control, circles 7−9).

gradient (Figure 1), where it reacted with O_2 from the aerobic zone. $Mn(II)_{aq}$ oxidation at the oxic−anoxic transition caused the accumulation of dark, reducible Mn precipitates dominated by Mn(III) phases (Figure 2, Figure 5, Table 1, Figure S-3). The formation of Mn(III) phases coincided with greater oxidation of lignin analogues (Figure 3a), as well as the solubilization and oxidation of POC within the transition zone (Figure 3b, Figure 5). The fact that both bulk measurements and micron-scale imaging show consistent patterns strongly suggests a causal link between POC degradation, $Mn(II)_{aq}$ oxidation, and Mn(III) generation at oxic−anoxic interfaces in subsurface environments.

Drivers of Mn(II) Oxidation at the Oxic−Anoxic Interface. Our measurements showed that overlapping gradients of dissolved O_2 and $Mn(II)_{aq}$ created a narrow zone in which $Mn(II)_{aq}$ oxidation occurred (Figure 1). This result is consistent with observations of fungal $Mn(II)_{aq}$ oxidation at the oxic−anoxic transitions, which resulted in the generation of Mn(III,IV) phases at the interface.[21] While this experiment was not designed to isolate Mn oxidation pathways, we observed heavy fungal growth within the transition zone (Figure S-2). Ascomycetes and Basidiomycetes, which are both fungal groups known to contain members with Mn-oxidizing potential,[12,15,17] are abundant in soils used for this study.[40] Abiotic $Mn(II)_{aq}$ oxidation by O_2 in the presence of suitable ligands, found to only occur at pH values greater than 7,[41] represents an unlikely pathway given our low soil pH of 4.1 in this study. An alternative abiotic pathway is $Mn(II)_{aq}$ oxidation through reactive oxygen species,[42] which may be created along the interface as a consequence of Fe(II)-driven Fenton reactions.[43] While we cannot exclude this possibility, the fact that no significant amounts of $Fe(II)_{aq}$ were found in the transition zone (Figure 1) suggest that it constitutes a minor pathway. Consequently, we conclude that the accumulation of oxidized Mn species along the oxic−anoxic interface is most likely the result of biotic $Mn(II)_{aq}$ oxidation. Resolving whether $Mn(II)_{aq}$ oxidation in soils is indeed driven by fungi or perhaps by Mn-oxidizing bacteria, and if biotic $Mn(II)_{aq}$ oxidation is mediated directly by enzymes[12] or indirectly through reactive intermediates,[17] warrants further research.

The Formation of Reactive Mn Species at Oxic−Anoxic Interfaces. $Mn(II)_{aq}$ oxidation at the oxic−anoxic interface resulted in the accumulation of dark, Mn(III)-dominated precipitates (Figure 2, Figure 4b). Thompson et al.[21] found similar Mn precipitates along oxic−anoxic transitions, which were found to consist of mixed-valence Mn(III,IV) oxides. In our system, LCFs of Mn XANES suggest that the accumulation of Mn(IV) is limited. The lack of Mn(IV) indicates that Mn(III) species formed upon $Mn(II)_{aq}$ oxidation were stabilized by suitable ligands. The POC and its degradation products in our system likely provided a sufficient amount of carboxylated and noncarboxylated ligands[41] capable of complexing and stabilizing Mn(III) upon formation, thus preventing the formation of Mn(IV). It is also possible that any Mn(IV) formed was promptly rereduced to Mn(III) and Mn(II)

DOI: 10.1021/acs.est.8b03791
Environ. Sci. Technol. 2018, 52, 12349−12357

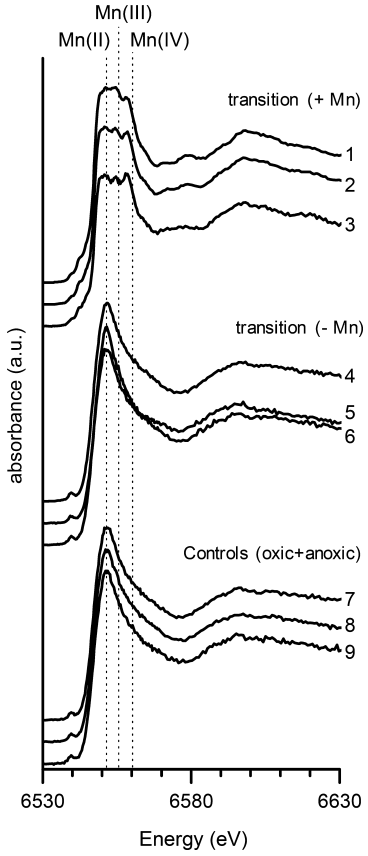

Figure 5. Mn μ-XANES spectra collected across the interface. Spectra were collected at Mn-rich (+Mn) and Mn-depleted (−Mn) locations within the transition zone, as well as locations in the oxic and anoxic zone (controls). Exact locations are identified by white circles in Figure 4b. Corresponding C XANES spectra are shown in Figure S-3.

by organic reducing agents in this C-rich environment.[44] We had previously found similarly Mn(III)-rich precipitates to accumulate during fungal degradation of POC in a forest soil,[14] which we attributed to the enzymatic formation of Mn(III)−ligand complexes during oxidative degradation. Although we were not able to quantify dissolved Mn(III)−ligand complexes directly in the present study due to the high organic C background in the pore water, the predominance of Mn(III) is consistent with the formation of dissolved Mn(III) species at oxic−anoxic interfaces as reported by Madison et al.[18] Further research should investigate the exact nature and reactivity of Mn(III) phases formed at these interfaces and the conditions that favor their formation.

Mn(III) Formation along the Interface Drives POC Degradation. Enhanced solubilization of organic compounds at the interface (Figure 3b) is in good agreement with the depolymerization of insoluble macromolecules to soluble products as mediated by Mn(III)−ligand complexes[12] or Mn(III/IV) oxide.[13] Elevated oxidation potential of lignin analogues (Figure 3a) and the observed decrease in aromatic C (Figure 3c and Table 1) is consistent with increased degradation of lignin in association with $Mn(II)_{aq}$ oxidation.[14] The observed increase in carboxyl C (Figure 3c, Table 1) suggests oxidation of aromatic side groups often observed during lignin decomposition, such as the oxidation of phenyl-aldehydes to carboxylic groups.[12] Oxidation of aromatic rings may generate unstable free radicals and lead to spontaneous ring cleavage,[12] which could be responsible for the decrease in aromaticity. Because depolymerization, solubilization, and oxidation are rate-limiting steps in the microbial degradation of POC to CO_2,[45] these Mn-mediated reactions in association with increased fungal growth at the interface are likely to increase overall oxidation rates and thus CO_2 emissions from soils.

The Significance of Mn in POC Oxidation at Oxic−Anoxic Interface. Although our results suggest the existence of a zone in which $Mn(II)_{aq}$ oxidation is spatially separate from that of $Fe(II)_{aq}$ oxidation, we cannot entirely exclude the role of $Fe(II)_{aq}$-mediated POC oxidation[38,39] in our system. It is possible that Fenton reactions produced reactive oxygen species at the base of the oxic zone, and that such species could have diffused upward into the transition zone to participate in enhanced POC oxidation. However, this transition zone showed greater accumulation of Mn than Fe oxide precipitates (Figure S-3), suggesting that the rate of $Mn(II)_{aq}$ oxidation was significantly larger than that of $Fe(II)_{aq}$ oxidation. $Fe(II)_{aq}$ supply toward the interface, and resulting Fe(III) oxide accumulation, may have been limited due to the short incubation time. Thermodynamics favor anaerobic microbial respiration of Mn(III,IV) oxides over that of Fe(III) oxides, and so reductive dissolution in the anaerobic zone may have supplied more $Mn(II)_{aq}$ than $Fe(II)_{aq}$ to the transition zone over the short experimental period. This scenario is analogous to forest soil surface layers that may experience oxygen gradients steep enough to result in Mn redox cycling,[23] but redox potentials may not be low enough or sufficiently stable to support Fe redox cycling. Further, organic surface layers in forest soils with high POC content are frequently enriched in Mn relative to Fe.[46] Under these environmental conditions, Mn(II) oxidation along oxic−anoxic transition may be a central control on POC oxidation. Conversely, in soils and sediments with higher Fe concentrations along with steeper and more stable redox gradients, Fe(II)-mediated POC oxidation may become more important.[38,39] This potential dichotomy between soil and sediment systems in which POC oxidation at oxic−anoxic interfaces is mediated by Mn and those in which Fe is dominant opens up interesting opportunities for future research.

Environmental Implications. Oxic−anoxic interfaces are ubiquitous in soil and sediment environments and are increasingly recognized as hotspots of C oxidation, but the role of Mn redox cycling in facilitating C oxidation has not been explored. This model-system study shows that enhanced C oxidation at oxic−anoxic interfaces is, at least in part, due to $Mn(II)_{aq}$ oxidation and the formation of Mn(III)-dominated precipitates. Depolymerization and oxidation of aromatic C was greatest at the oxic−anoxic interface and corresponded with biotic $Mn(II)_{aq}$ oxidation, creating a narrow band in which reactive Mn(III) phases were formed. Microscale imaging confirmed that hotspots of Mn(III) formation at the interface coincided with the presence of oxidized POC. Our combination of macro- and microscale analyses suggest that biotic $Mn(II)_{aq}$ oxidation at oxic−anoxic interfaces, fueled by readily available oxygen and $Mn(II)_{aq}$, are a key driver of POC oxidation. These results indicate that POC oxidation is not merely a function of molecular composition or nutrient availability,[3] which insufficiently predicts rates,[47] but is dependent on microenvironments favoring the formation of critically important oxidants such as Mn(III). The importance of Mn(III)-mediated POC oxidation may have broad implications for C storage and the fate of natural and xenobiotic compounds in other environments with ubiquitous oxic−anoxic

DOI: 10.1021/acs.est.8b03791
Environ. Sci. Technol. 2018, 52, 12349−12357

boundaries, such as wetlands, sediments, peatlands, and groundwater aquifers.

■ ASSOCIATED CONTENT

Supporting Information

The Supporting Information is available free of charge on the ACS Publications website at DOI: 10.1021/acs.est.8b03791.

Tables S1−S3, Figures S1−S4 (PDF)

■ AUTHOR INFORMATION

Corresponding Author

*Address: School of Earth & Sustainability, Stockbridge School of Agriculture, University of Massachusetts, Amherst, 162 Holdsworth Way, Amherst, MA 01003. E-mail: Keiluweit@umass.edu.

ORCID

Samantha Ying: 0000-0002-1247-2529

Marco Keiluweit: 0000-0002-7061-8346

Notes

The authors declare no competing financial interest.

■ ACKNOWLEDGMENTS

The authors would like to thank the Harvard Forest LTER personnel and REU students Sarah Pardi and Megan Wilcots. C XANES spectroscopy reported in this paper was performed at the Canadian Light Source (CLS), which is supported by the Canada Foundation for Innovation, Natural Sciences and Engineering Research Council of Canada, the University of Saskatchewan, the Government of Saskatchewan, Western Economic Diversification Canada, the National Research Council Canada, and the Canadian Institutes of Health Research. This research used beamline SRX (5-ID) of the National Synchrotron Light Source II, a U.S. Department of Energy (DOE) Office of Science User Facility operated for the DOE Office of Science by Brookhaven National Laboratory under contract no. DE-SC0012704. Use of SSRL at the Stanford Linear Accelerator Center National Accelerator Laboratory is supported by the U.S. Department of Energy, Office of Science, Office of Basic Energy Sciences under contract DE-AC02-76SF00515. S.C.Y. was supported by USDA National Institute of Food and Agriculture, Hatch project CA-R-ENS-5151-H. This work was supported by the Department of Energy, Office of Biological and Environmental Research, Subsurface Biosphere Research program (award no. DE-SC0016544), the Harvard Forest LTER program (award no. NSF-DEB 1237491), and the University of Massachusetts.

■ REFERENCES

(1) Liang, C.; Schimel, J. P.; Jastrow, J. D. The Importance of Anabolism in Microbial Control over Soil Carbon Storage. *Nature Microbiology* **2017**, *2* (8), 17105.

(2) Heimann, M.; Reichstein, M. Terrestrial Ecosystem Carbon Dynamics and Climate Feedbacks. *Nature* **2008**, *451* (7176), 289−292.

(3) Meentemeyer, V. Macroclimate the Lignin Control of Litter Decomposition Rates. *Ecology* **1978**, *59* (3), 465−472.

(4) Turner, S.; Gallois, P.; Brown, D. Tracheary Element Differentiation. *Annu. Rev. Plant Biol.* **2007**, *58*, 407−433.

(5) Heim, A.; Frey, B. Early Stage Litter Decomposition Rates for Swiss Forests. *Biogeochemistry* **2004**, *70* (3), 299−313.

(6) Berg, B.; Erhagen, B.; Johansson, M.-B.; Nilsson, M.; Stendahl, J.; Trum, F.; Vesterdal, L. Manganese in the Litter Fall-Forest Floor Continuum of Boreal and Temperate Pine and Spruce Forest Ecosystems − A Review. *For. Ecol. Manage.* **2015**, *358*, 248−260.

(7) De Marco, A.; Spaccini, R.; Vittozzi, P.; Esposito, F.; Berg, B.; Virzo De Santo, A. Decomposition of Black Locust and Black Pine Leaf Litter in Two Coeval Forest Stands on Mount Vesuvius and Dynamics of Organic Components Assessed through Proximate Analysis and NMR Spectroscopy. *Soil Biol. Biochem.* **2012**, *51*, 1−15.

(8) Aponte, C.; García, L. V.; Marañón, T. Tree Species Effect on Litter Decomposition and Nutrient Release in Mediterranean Oak Forests Changes Over Time. *Ecosystems* **2012**, *15* (7), 1204−1218.

(9) Berg, B.; Steffen, K. T.; McClaugherty, C. Litter Decomposition Rate Is Dependent on Litter Mn Concentrations. *Biogeochemistry* **2007**, *82* (1), 29−39.

(10) Trum, F.; Titeux, H.; Cornelis, J.-T.; Delvaux, B. Effects of Manganese Addition on Carbon Release from Forest Floor Horizons. *Can. J. For. Res.* **2011**, *41* (3), 643−648.

(11) Perez, J.; Jeffries, T. W. Roles of Manganese and Organic Acid Chelators in Regulating Lignin Degradation and Biosynthesis of Peroxidases by Phanerochaete Chrysosporium. *Appl. Environ. Microbiol.* **1992**, *58* (8), 2402−2409.

(12) Hofrichter, M. Review: Lignin Conversion by Manganese Peroxidase (MnP). *Enzyme Microb. Technol.* **2002**, *30* (4), 454−466.

(13) Sunda, W. G.; Kieber, D. J. Oxidation of Humic Substances by Manganese Oxides Yields Low-Molecular-Weight Organic Substrates. *Nature* **1994**, *367* (6458), 62−64.

(14) Keiluweit, M.; Nico, P.; Harmon, M. E.; Mao, J.; Pett-Ridge, J.; Kleber, M. Long-Term Litter Decomposition Controlled by Manganese Redox Cycling. *Proc. Natl. Acad. Sci. U. S. A.* **2015**, *112* (38), E5253−E5260.

(15) Tebo, B. M.; Johnson, H. A.; McCarthy, J. K.; Templeton, A. S. Geomicrobiology of Manganese(II) Oxidation. *Trends Microbiol.* **2005**, *13* (9), 421−428.

(16) Andeer, P. F.; Learman, D. R.; McIlvin, M.; Dunn, J. A.; Hansel, C. M. Extracellular Haem Peroxidases Mediate Mn(II) Oxidation in a Marine Roseobacter Bacterium via Superoxide Production. *Environ. Microbiol.* **2015**, *17* (10), 3925−3936.

(17) Hansel, C. M.; Zeiner, C. A.; Santelli, C. M.; Webb, S. M. Mn(II) Oxidation by an Ascomycete Fungus Is Linked to Superoxide Production during Asexual Reproduction. *Proc. Natl. Acad. Sci. U. S. A.* **2012**, *109* (31), 12621−12625.

(18) Madison, A. S.; Tebo, B. M.; Mucci, A.; Sundby, B.; Luther, G. W. Abundant Porewater Mn(III) Is a Major Component of the Sedimentary Redox System. *Science* **2013**, *341* (6148), 875−878.

(19) Oldham, V. E.; Owings, S. M.; Jones, M. R.; Tebo, B. M.; Luther, G. W., III Evidence for the Presence of Strong Mn(III)-Binding Ligands in the Water Column of the Chesapeake Bay. *Mar. Chem.* **2015**, *171*, 58−66.

(20) Oldham, V. E.; Mucci, A.; Tebo, B. M.; Luther, G. W. Soluble Mn(III)−L Complexes Are Abundant in Oxygenated Waters and Stabilized by Humic Ligands. *Geochim. Cosmochim. Acta* **2017**, *199*, 238−246.

(21) Thompson, I. A.; Huber, D. M.; Guest, C. A.; Schulze, D. G. Fungal Manganese Oxidation in a Reduced Soil. *Environ. Microbiol.* **2005**, *7* (9), 1480−1487.

(22) Keiluweit, M.; Nico, P. S.; Kleber, M.; Fendorf, S. Are Oxygen Limitations under Recognized Regulators of Organic Carbon Turnover in Upland Soils? *Biogeochemistry* **2016**, *127* (2), 157−171.

(23) van der Lee, G. E. M.; de Winder, B.; Bouten, W.; Tietema, A. Anoxic Microsites in Douglas Fir Litter. *Soil Biol. Biochem.* **1999**, *31* (9), 1295−1301.

(24) Jost, D.; Haberer, C. M.; Grathwohl, P.; Winter, J.; Gallert, C. Oxygen Transfer in a Fluctuating Capillary Fringe: Impact of Microbial Respiratory Activity. *Vadose Zone J.* **2015**, *14* (5), 0.

(25) Rezanezhad, F.; Couture, R.-M.; Kovac, R.; O'Connell, D.; Van Cappellen, P. Water Table Fluctuations and Soil Biogeochemistry: An Experimental Approach Using an Automated Soil Column System. *J. Hydrol.* **2014**, *509*, 245−256.

(26) Winter, J.; Ippisch, O.; Vogel, H.-J. Dynamic Processes in Capillary Fringes. *Vadose Zone J.* **2015**, *14* (5), 0.

(27) Keiluweit, M.; Wanzek, T.; Kleber, M.; Nico, P.; Fendorf, S. Anaerobic Microsites Have an Unaccounted Role in Soil Carbon Stabilization. *Nat. Commun.* **2017**, *8* (1), 1771.
(28) Luther, G. W., III; Glazer, B. T.; Ma, S.; Trouwborst, R. E.; Moore, T. S.; Metzger, E.; Kraiya, C.; Waite, T. J.; Druschel, G.; Sundby, B.; et al. Use of Voltammetric Solid-State (Micro)Electrodes for Studying Biogeochemical Processes: Laboratory Measurements to Real Time Measurements with an in Situ Electrochemical Analyzer (ISEA). *Mar. Chem.* **2008**, *108* (3−4), 221−235.
(29) Phillips, S. C.; Varner, R. K.; Frolking, S.; Munger, J. W.; Bubier, J. L.; Wofsy, S. C.; Crill, P. M. Interannual, Seasonal, and Diel Variation in Soil Respiration Relative to Ecosystem Respiration at a Wetland to Upland Slope at Harvard Forest. *J. Geophys. Res.* **2010**, *115* (G2), G02019.
(30) Bristow, G.; Taillefert, M. VOLTINT: A Matlab ®-Based Program for Semi-Automated Processing of Geochemical Data Acquired by Voltammetry. *Comput. Geosci.* **2008**, *34*, 153−162.
(31) Brendel, P. J.; Luther, G. W. I. Development of a Gold Amalgam Voltammetric Microelectrode for the Determination of Dissolved Fe, Mn, O2, and S(-II) in Porewaters of Marine and Freshwater Sediments. *Environ. Sci. Technol.* **1995**, *29* (3), 751−761.
(32) Chao, T. T. Selective Dissolution of Manganese Oxides from Soils and Sediments with Acidified Hydroxylamine Hydrochloride 1. *Soil Science Society of America Journal* **1972**, *36* (5), 764−768.
(33) Guest, C. A.; Schulze, D. G.; Thompson, I. A.; Huber, D. M. Correlating Manganese X-Ray Absorption near-Edge Structure Spectra with Extractable Soil Manganese. *Soil Sci. Soc. Am. J.* **2002**, *66* (4), 1172−1181.
(34) Bach, C. E.; Warnock, D. D.; Van Horn, D. J.; Weintraub, M. N.; Sinsabaugh, R. L.; Allison, S. D.; German, D. P. Measuring Phenol Oxidase and Peroxidase Activities with Pyrogallol, l-DOPA, and ABTS: Effect of Assay Conditions and Soil Type. *Soil Biol. Biochem.* **2013**, *67*, 183−191.
(35) Manceau, A.; Marcus, M. A.; Grangeon, S. Determination of Mn Valence States in Mixed-Valent Manganates by XANES Spectroscopy. *Am. Mineral.* **2012**, *97* (5−6), 816−827.
(36) Regier, T.; Krochak, J.; Sham, T. K.; Hu, Y. F.; Thompson, J.; Blyth, R. I. R. Performance and Capabilities of the Canadian Dragon: The SGM Beamline at the Canadian Light Source. *Nucl. Instrum. Methods Phys. Res., Sect. A* **2007**, *582* (1), 93−95.
(37) Canfield, D. E.; Thamdrup, B.; Hansen, J. W. The Anaerobic Degradation of Organic Matter in Danish Coastal Sediments: Iron Reduction, Manganese Reduction, and Sulfate Reduction. *Geochim. Cosmochim. Acta* **1993**, *57* (16), 3867−3883.
(38) Hall, S. J.; Silver, W. L. Iron Oxidation Stimulates Organic Matter Decomposition in Humid Tropical Forest Soils. *Glob Change Biol.* **2013**, *19* (9), 2804−2813.
(39) Wang, Y.; Wang, H.; He, J.-S.; Feng, X. Iron-Mediated Soil Carbon Response to Water-Table Decline in an Alpine Wetland. *Nat. Commun.* **2017**, *8*, 15972.
(40) Morrison, E. W.; Frey, S. D.; Sadowsky, J. J.; van Diepen, L. T. A.; Thomas, W. K.; Pringle, A. Chronic Nitrogen Additions Fundamentally Restructure the Soil Fungal Community in a Temperate Forest. *Fungal Ecology* **2016**, *23*, 48−57.
(41) Duckworth, O. W.; Sposito, G. Siderophore−Manganese(III) Interactions. I. Air-Oxidation of Manganese(II) Promoted by Desferrioxamine B. *Environ. Sci. Technol.* **2005**, *39* (16), 6037−6044.
(42) Nico, P. S.; Anastasio, C.; Zasoski, R. J. Rapid Photo-Oxidation of Mn(II) Mediated by Humic Substances. *Geochim. Cosmochim. Acta* **2002**, *66* (23), 4047−4056.
(43) Jia, M.; Bian, X.; Yuan, S. Production of Hydroxyl Radicals from Fe(II) Oxygenation Induced by Groundwater Table Fluctuations in a Sand Column. *Sci. Total Environ.* **2017**, *584−585*, 41−47.
(44) Stone, A. T.; Morgan, J. J. Reduction and Dissolution of Manganese (III) and Manganese (IV) Oxides by Organics: 2. Survey of the Reactivity of Organics. *Environ. Sci. Technol.* **1984**, *18* (8), 617−624.
(45) Lehmann, J.; Kleber, M. The Contentious Nature of Soil Organic Matter. *Nature* **2015**, *528* (7580), 60−68.
(46) Kaste, J. M.; Bostick, B. C.; Heimsath, A. M.; Steinnes, E.; Friedland, A. J. Using Atmospheric Fallout to Date Organic Horizon Layers and Quantify Metal Dynamics during Decomposition. *Geochim. Cosmochim. Acta* **2011**, *75* (6), 1642−1661.
(47) Bradford, M. A.; Berg, B.; Maynard, D. S.; Wieder, W. R.; Wood, S. A. Understanding the Dominant Controls on Litter Decomposition. *J. Ecol.* **2016**, *104* (1), 229−238.

DOI: 10.1021/acs.est.8b03791
Environ. Sci. Technol. 2018, 52, 12349−12357